

A Quantum Gas Microscope for Fermionic Atoms

Lawrence W. Cheuk, Matthew A. Nichols, Melih Okan, Thomas Gersdorf,
Vinay V. Ramasesh, Waseem S. Bakr, Thomas Lompe, Martin W. Zwierlein¹

¹*Department of Physics, MIT-Harvard Center for Ultracold Atoms, and
Research Laboratory of Electronics, MIT, Cambridge, Massachusetts 02139, USA*

Strongly interacting fermions define the properties of complex matter at all densities, from atomic nuclei to modern solid state materials and neutron stars. Ultracold atomic Fermi gases have emerged as a pristine platform for the study of many-fermion systems. Here we realize a quantum gas microscope for fermionic ^{40}K atoms trapped in an optical lattice, which allows one to probe strongly correlated fermions at the single atom level. We combine 3D Raman sideband cooling with high-resolution optics to simultaneously cool and image individual atoms with single lattice site resolution at a detection fidelity above 95%. The imaging process leaves each atom predominantly in the 3D ground state of its lattice site, inviting the implementation of a Maxwell's demon to assemble low-entropy many-body states. Single site resolved imaging of fermions enables the direct observation of magnetic order, time resolved measurements of the spread of particle correlations, and the detection of many-fermion entanglement.

The collective behavior of fermionic particles governs the structure of the elements, the workings of high-temperature superconductors and colossal magnetoresistance materials, and the properties of nuclear matter. Yet, our understanding of strongly interacting Fermi systems is limited, due in part to the antisymmetry requirement on the many-fermion wavefunction and the resulting “fermion sign problem”. In recent years, ultracold atomic quantum gases have enabled quantitative experimental tests of theories of strongly interacting fermions [1–4]. In particular, fermions trapped in optical lattices can directly simulate the physics of electrons in a crystalline solid, shedding light on novel physical phenomena in materials with strong electron correlations. A major effort is devoted to the realization of the Fermi-Hubbard model at low entropies, believed to capture the essential aspects of high- T_c superconductivity [5–11]. For bosonic atoms, a new set of experimental probes ideally suited for the observation of magnetic order and correlations became available with the advent of quantum gas microscopes [12–14], the high-resolution imaging of Hubbard-type lattice systems at the single atom level. It allowed the direct observation of spatial structures and ordering in the Bose-Hubbard model [13, 15] and of the intricate correlations and dynamics in these systems [16, 17]. A long-standing goal has been to realize such a quantum gas microscope for fermionic atoms. It would allow the direct observation and control at the single lattice site level of strongly correlated fermion systems, in particular the Fermi-Hubbard model, in regimes that cannot be described by current theories. These prospects have sparked significant experimental effort to realize site-resolved, high-fidelity imaging of ultracold fermions, but this goal has so far remained elusive.

In the present work, we realize a quantum gas microscope for fermionic ^{40}K atoms. To achieve high resolution imaging, the setup incorporates a hemispherical

solid immersion lens optically contacted to the vacuum window (Fig. 1(a)). In combination with a microscope objective with $\text{NA} = 0.60$, the system achieves an enhanced NA of 0.87 while eliminating aberrations that would arise from a planar vacuum window. In order to keep the atoms localized while performing fluorescence imaging, one must simultaneously cool them in order to mitigate the heating from spontaneously emitted imaging photons. Previous microscope experiments [12–14] cool via optical molasses. In contrast, we combine high-resolution imaging with continuous 3D Raman sideband cooling [18–24], in which Raman transitions on vibration-lowering sidebands are combined with optical pumping to provide cooling. Our method therefore achieves not only site-resolved imaging, but it also leaves a large fraction of the atoms (73%) in the 3D motional ground state of each lattice site. This opens up the prospects to prepare low entropy many-body states by measuring the initial positions of the atoms and rearranging them into the desired configuration [25].

Raman sideband cooling has previously been used to cool atoms in lattices and in optical tweezers to large ground state populations in ^{87}Rb and ^{133}Cs [18–24]. Our cooling scheme uses two states from the two ground hyperfine manifolds, $|a\rangle = |9/2, -9/2\rangle$ and $|b\rangle = |7/2, -7/2\rangle$, to form an effective two-level system. To make $|a\rangle$ and $|b\rangle$ non-degenerate with other hyperfine states, and to provide a quantization axis for optical pumping, we apply a bias field of 4.2 G along the x direction (Fig 1(b)). A pair of Raman beams collinear with the x and y lattice beams, but not retro-reflected, drives vibration-lowering Raman transitions from $|a\rangle$ to $|b\rangle$ (Fig. 1(c)). The Raman lasers are detuned -41 GHz from the D2 line. The optical pumping is performed on the D1 line, 3 nm away from the D2 line, allowing us to filter out stray Raman light while transmitting atomic fluorescence. By collecting the spontaneously scattered photons during this optical pumping process, we can im-

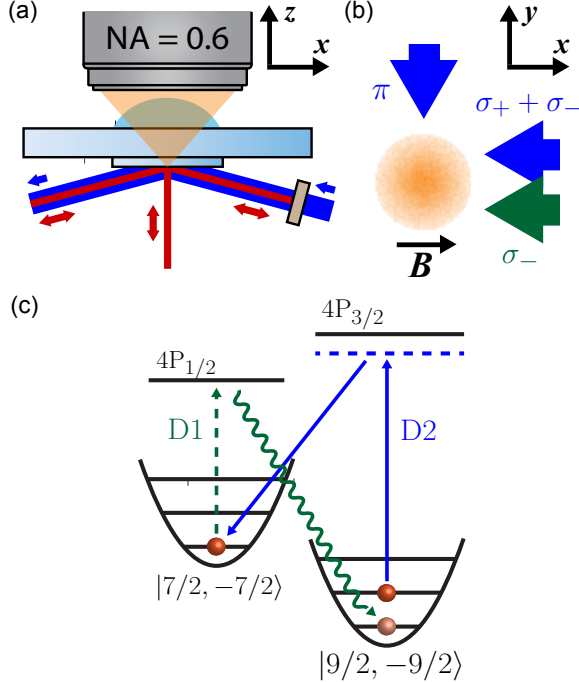


FIG. 1. (a) High-resolution imaging setup. The solid immersion lens consists of a hemispherical cap and a super-polished substrate contacted on either side of the vacuum window. Combined with an objective with numerical aperture of $NA = 0.60$, the system achieves an effective $NA = 0.87$. The substrate reflects 1064 nm light while transmitting D1 and D2 light of ^{40}K . The lattice beams are shown in red; the optical pumping and x -Raman beams are shown in blue. (b) Top view of Raman beams (blue) and optical pumping beam (green). (c) Raman cooling scheme. The Raman beams detuned near the D2 line (solid blue) drive vibration-lowering transitions. The optical pumping beam (dashed green) is tuned to the D1 line.

age the atoms without using additional resonant light.

To prepare a cold cloud of fermionic atoms under the microscope, ^{40}K is first sympathetically cooled with ^{23}Na in a plugged magnetic quadrupole trap [26], centered ~ 9 mm below a super-polished substrate that forms the flat part of the hemispherical immersion lens. After removal of ^{23}Na , the cloud of ~ 1 million ^{40}K atoms is magnetically transported to the substrate and trapped in a vertical lattice formed by a 1064 nm laser beam reflected off the substrate under an angle of 5.9° . A single layer $7.8\ \mu\text{m}$ from the surface is selected using a radiofrequency sweep in a vertical magnetic gradient followed by a resonant light pulse that removes atoms in the remaining layers. Next, we prepare a 50/50 mixture of $|F = 9/2, m_F = -9/2\rangle$ and $|9/2, -7/2\rangle$ to allow thermalization, and transfer the atoms to a vertical (z direction) 1064 nm beam, forming a lattice along z with 532 nm spacing (Fig. 1(a)). After evaporating by lowering the power of the z -lattice, the z -depth is increased to $180\ \mu\text{K}$. We simultaneously turn on two additional

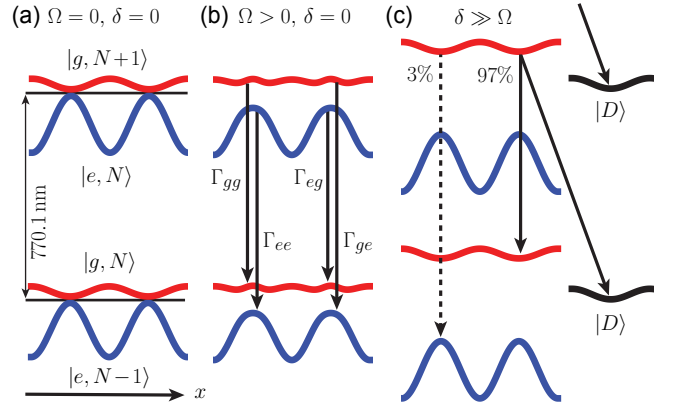


FIG. 2. (a) Effect of the optical lattice on the electronic ground ($|g\rangle$) and excited ($|e\rangle$) states. $|g\rangle$ is trapping; $|e\rangle$ is anti-trapping. (b) For resonant drive, all dressed states are equally populated and experience an anti-trapping potential. The four decay channels between the dressed states are all equal. (c) Dressed states with $\Omega/\delta = 0.175$, along with dark state ($|D\rangle$). Only a small fraction Ω^4/δ^4 of the steady-state population resides in anti-trapping states. Shown are the decay channels out of the trapping state, with the branching ratio between trapping transitions (solid arrow) to anti-trapping transitions (dashed arrow).

1064 nm beams (Fig. 1(a)) reflected off the substrate at 10.8° and retro-reflected. These form a lattice in the horizontal plane with spacing 541 nm.

During imaging, the atoms are trapped in a deep lattice, where the potential at each lattice site can be approximated by a harmonic well with vibrational frequency ω . At our imaging depth, the vibrational frequencies for the three axes are $\omega_x = 2\pi \times 280\ \text{kHz}$, $\omega_y = 2\pi \times 300\ \text{kHz}$, and $\omega_z = 2\pi \times 260\ \text{kHz}$, corresponding to lattice depths of $210\ \mu\text{K}$, $240\ \mu\text{K}$ and $180\ \mu\text{K}$ respectively. The Rabi coupling for transitions that change vibrational number by one is proportional to the Lamb-Dicke parameter, $\eta = \Delta k a$, where $a = \sqrt{\frac{\hbar}{2m\omega}}$ is the oscillator length and $\hbar\Delta k$ is the momentum transfer due to the Raman beams. Along our lattice directions, $\Delta k_x = 8.0\ \mu\text{m}^{-1}$, $\Delta k_y = 8.0\ \mu\text{m}^{-1}$ and $\Delta k_z = 3.1\ \mu\text{m}^{-1}$, yielding Lamb-Dicke parameters of 0.17 for x and y , and 0.068 for z . The polarizations of both Raman beams are linear and parallel to the substrate (Fig. 1(b)), in order to avoid differential effective magnetic fields between $|a\rangle$ and $|b\rangle$ that would arise for circularly polarized light. The Raman beam along the y -axis contains a single frequency, whereas the Raman beam along the x -axis contains three frequencies, allowing us to address the cooling sidebands of three directions simultaneously. The resulting two-photon detunings from the bare $|a\rangle \rightarrow |b\rangle$ transition are 400 kHz, 450 kHz and 360 kHz for cooling along x , y and z respectively. These frequencies compensate for differential Stark shifts that arise in the presence of optical pumping light. The x -Raman beam intensi-

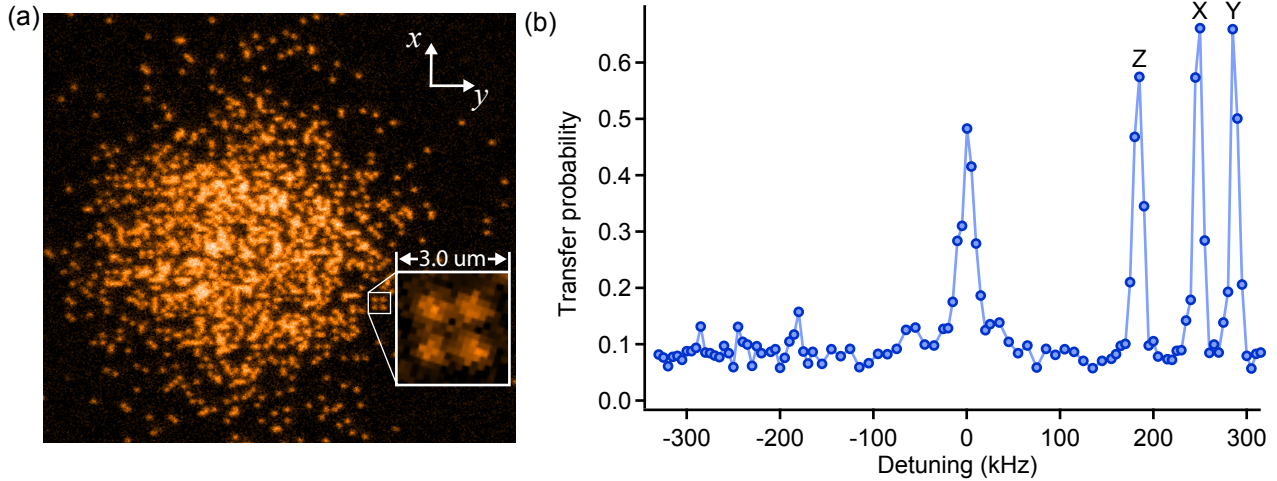


FIG. 3. (a) Site-resolved imaging of fermionic atoms on a densely-filled 541 nm-period optical lattice; one can clearly discern the lattice structure and individual atoms. (b) Raman spectrum after cooling. The lattice depths are chosen such that the vibrational sidebands are clearly separated. The heating sidebands for the three lattice axes are labeled Z, X and Y. We observe a large sideband asymmetry, from which we extract a 3D ground state occupation of 73%.

ties of the three frequency components are 0.79 W/cm², 0.47 W/cm² and 0.49 W/cm² respectively; the intensity of the y -Raman beam is 2.0 W/cm².

In addition to these Raman beams, the optical pumping light is present to complete the cooling cycle. During optical pumping, atoms enter electronically excited states, and preferentially decay into the desired state. Generally, the excited states experience an anti-trapping potential when the ground state experiences a trapping potential. For our 1064 nm lattice, the anti-trapping potential for the atoms in the $4\text{P}_{1/2}$ states is 5.4 times stronger than the trapping potential for atoms in the $4\text{S}_{1/2}$ states, due to the $4\text{P}_{1/2}$ to $3\text{D}_{3/2}$ transition at 1169 nm. This strong anti-trapping would typically lead to heating and diffusion of atoms through the lattice during imaging.

A solution to this problem is to detune the optical pumping light away from resonance. This can be understood by considering the dressed states of a driven two-level system where the excited state is anti-trapping and the ground state is trapping. At large detunings, the dressed states, $|g, N\rangle$ and $|e, N\rangle$, correspond to the bare trapping and anti-trapping states with N photons respectively (Fig 2(a)). Spontaneous emission leads to decays of $|e, N\rangle \rightarrow |g, N\rangle$, $|e, N\rangle \rightarrow |e, N-1\rangle$, $|g, N+1\rangle \rightarrow |g, N\rangle$ and $|g, N+1\rangle \rightarrow |e, N-1\rangle$, with rates Γ_{eg} , Γ_{ee} , Γ_{gg} and Γ_{ge} respectively. On resonance, where both dressed states are anti-trapping, these four rates are equal, and thus the populations in the two dressed states are also equal (Fig. 2(b)).

However, at large detunings $\delta \gg \Omega$, where Ω is the Rabi frequency, the situation is very different. One dressed state becomes trapping and the decay rates between the states are no longer equal. Specifically, they

are proportional to 1, s , s and s^2 respectively, where $s = \Omega^2/\delta^2$. The asymmetry of these rates at large δ reduces the effects of the remaining anti-trapping states via two mechanisms. The first is suppression of population in the anti-trapping states. In steady state, the ratio of the anti-trapped population to the trapped population is given by Γ_{ge}/Γ_{eg} , which at large detunings scales as s^2 .

To understand the second mechanism, one must also consider the state $|D\rangle$ into which atoms are optically pumped (Fig. 2(c)). This state is dark to the optical pumping light, and hence has no excited state admixture; consequently, it experiences a trapping potential. At large detunings, atoms decay from the trapped and anti-trapped states into the dark state with rates proportional to Γ_{gg} and Γ_{eg} , respectively, to lowest order in s . For atoms in a trapping state $|g, N\rangle$, the ratio of anti-trapping transitions to dark state transitions scales as $\Gamma_{ge}/\Gamma_{gg} = s$, showing that anti-trapping transitions are suppressed relative to the desired transitions into the dark state. For the small fraction s^2 of atoms in an anti-trapping state $|e, N\rangle$, the ratio of anti-trapping transitions to trapping transitions scales as $\Gamma_{ee}/\Gamma_{eg} = s$, which indicates that these atoms are preferentially pumped into trapping states.

In light of these considerations, we detune the F -pumping light -80 MHz from the Stark-shifted $F = 7/2 \rightarrow F' = 9/2$ transition and the m_F -pumping light -80 MHz from the Stark-shifted $F = 9/2 \rightarrow F' = 7/2$ transition. The optical pumping beam co-propagates with the x -Raman beam, and has its polarization optimized for minimal σ_+ admixture. The F and m_F components have intensities of 5.8 mW/cm² and 1.6 mW/cm² respectively; the Lamb-Dicke parameters for optical pumping are 0.17 for x and y , and 0.18 for z .

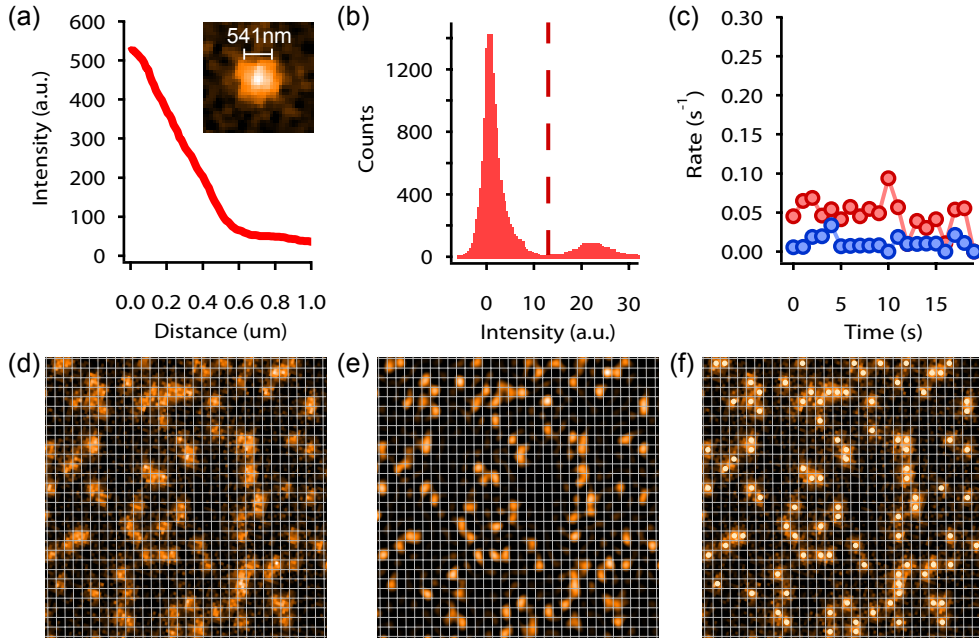


FIG. 4. (a) Radially averaged PSF extracted from isolated atoms; the FWHM is 640nm. (b) Intensity histogram after binning the deconvolved images by lattice site. The threshold for reconstruction is shown by the dashed line. (c) Loss and hopping rates, shown in red and blue circles respectively, as extracted from 20 consecutive 1-second images. (d) Image of sparsely filled lattice with grid lines showing lattice spacing and orientation. (e,f) The same image after deconvolution and with the filled sites identified.

This Raman cooling scheme allows us to collect fluorescence while keeping atoms confined to each lattice site (Fig. 3(a)). Furthermore, atoms are cooled predominantly into the 3D ground state, as verified with Raman spectroscopy (Fig. 3(b)). We measure a 3D ground state population of at least 73% after Raman cooling, where parameters are optimized for imaging fidelity rather than large ground state population. We measure a fluorescence rate of ~ 5000 photons/atom \cdot s with a lifetime of ~ 30 seconds. With a photon collection and detection efficiency of 20%, we can therefore collect ~ 1000 photons per atom in an exposure time of 1 second, which is sufficient to detect single atoms with high fidelity. Using the number of scattered photons and the Lamb-Dicke parameters for spontaneous emission, we estimate a cooling rate of $\sim 4 \mu\text{K}/\text{ms}$.

To verify that we can resolve individual lattice sites, we measure the point spread function (PSF) of our imaging system using isolated atoms from sparsely populated images. The measured PSF has a FWHM of 640 nm (Fig. 4(a)). Despite the measured FWHM being larger than the lattice spacing of 541 nm, images can be deconvolved with the measured PSF to allow sub-lattice-site resolution. From such images, we also extract the lattice axes and spacings necessary to reconstruct the atomic distribution. Binning the intensity of the deconvolved image by lattice site reveals a clear bimodal distribution (Fig. 4(b)), which is used to determine whether a site is

filled (Fig. 4(d,e,f)). This bimodality gives a reconstruction error of $< 1\%$.

To confirm that atoms do not move or disappear during the exposure, we measure hopping and loss rates. This is done by taking a series of images of the same atomic cloud and observing changes in the site occupations between frames. Sites that are empty but become occupied in a subsequent frame are counted as hopping events; sites that become empty are counted as loss events. We optimize the Raman cooling parameters for low hopping rates and loss rates while maintaining a fixed level of fluorescence. For optimized parameters, we achieve loss rates of $< 4.8 \pm 0.2\%$ and hopping rates of $< 1.2 \pm 0.2\%$ for 1 second exposures of clouds with fillings between 0.10 and 0.20 (Fig. 4(c)). These rates, which include reconstruction errors, give a detection fidelity of $> 95\%$ for sparse clouds. At higher fillings we expect higher loss rates, since hopping events lead to loss of additional atoms in doubly-occupied sites due to light-assisted collisions. Taking this into account, we estimate a fidelity of $> 92\%$ for a system with unity filling.

To ensure that our imaging technique does not cause additional losses for neighboring atoms, we measure the 2-point correlation function $g_2(r) = \langle n(x)n(x+r) \rangle / \langle n \rangle^2$ of thermal clouds, since distance-dependent loss will show up as anti-correlation at short distances. The reconstructed density distribution allows us to measure $g_2(r)$ from a single frame. With a dilute thermal cloud with

a filling of 0.19, and a 29×32 site sample, we measure $g_2(r) = 1.00(7)$ for distances from $r = 1$ to 10 lattice spacings, indicating that the imaging does not exhibit distance-dependent loss.

In conclusion, we have realized high-fidelity site-resolved imaging of ^{40}K fermionic atoms in a Hubbard-type optical lattice by combining 3D Raman sideband cooling with high resolution photon collection. In contrast to existing boson microscopes, the technique leaves atoms predominantly in the absolute 3D ground state of a given lattice site. This opens up new ways to assemble low-entropy Fermi-Hubbard systems atom by atom [25, 27, 28]. Combining site-resolved imaging with on-site manipulation would allow to deterministically create localized excitations and follow their time evolution [17]. Finally, the presence of ^{23}Na in our system invites the realization of a quantum gas microscope for ultracold fermionic NaK molecules [29], which have been proposed as a new resource for quantum information processing and quantum simulation of lattice models with long-range dipolar interactions.

We would like to thank Katherine Lawrence for experimental assistance. This work was supported by the NSF, AFOSR-PECASE, AFOSR-MURI on Exotic Phases of Matter, ARO-MURI on Atomtronics, ONR, a grant from the Army Research Office with funding from the DARPA OLE program, and the David and Lucille Packard Foundation.

[1] M. Inguscio, W. Ketterle, and C. Salomon, eds., *Ultracold Fermi Gases*, Proceedings of the International School of Physics "Enrico Fermi", Course CLXIV, Varenna, 20 - 30 June 2006 (IOS Press, Amsterdam, 2008).

[2] I. Bloch, J. Dalibard, and W. Zwerger, Rev. Mod. Phys. **80**, 885 (2008).

[3] W. Zwerger, ed., *The BCS-BEC crossover and the unitary Fermi gas*, Vol. 836 (Springer, 2011).

[4] M. W. Zwierlein, in *Novel Superfluids*, Vol. 2, edited by K.-H. Bennemann and J. B. Ketterson (Oxford University Press, Oxford, 2014).

[5] T. Esslinger, Annual Review of Condensed Matter Physics **1**, 129 (2010).

[6] J. Chin, D. Miller, Y. Liu, C. Stan, W. Setiawan, C. Sanner, K. Xu, and W. Ketterle, Nature **443**, 961 (2006).

[7] R. Jördens, N. Strohmaier, K. Günter, H. Moritz, and T. Esslinger, Nature **455**, 204 (2008).

[8] U. Schneider, L. Hackermüller, S. Will, T. Best, I. Bloch, T. A. Costi, R. W. Helmes, D. Rasch, and A. Rosch, Science **322**, 1520 (2008).

[9] D. Greif, T. Uehlinger, G. Jotzu, L. Tarruell, and T. Esslinger, Science **340**, 1307 (2013).

[10] J. Imrika, M. Iazzi, L. Wang, E. Gull, D. Greif, T. Uehlinger, G. Jotzu, L. Tarruell, T. Esslinger, and M. Troyer, Phys. Rev. Lett. **112**, 115301 (2014).

[11] R. A. Hart, P. M. Duarte, T. L. Yang, X. X. Liu, T. Paiva, E. Khatami, R. Scalettar, N. Trivedi, D. A. Huse, and R. G. Hulet, Preprint arXiv:1407.5932 (2014).

[12] W. S. Bakr, J. I. Gillen, A. Peng, S. Fölling, and M. Greiner, Nature **462**, 74 (2009).

[13] J. F. Sherson, C. Weitenberg, M. Endres, M. Cheneau, I. Bloch, and S. Kuhr, Nature **467**, 68 (2010).

[14] M. Miranda, R. Inoue, Y. Okuyama, A. Nakamoto, and M. Kozuma, ArXiv e-prints (2014), arXiv:1410.5189.

[15] W. S. Bakr, A. Peng, M. E. Tai, R. Ma, J. Simon, J. I. Gillen, S. Fölling, L. Pollet, and M. Greiner, Science **329**, 547 (2010).

[16] M. Endres, M. Cheneau, T. Fukuhara, C. Weitenberg, P. Schauß, C. Gross, L. Mazza, M. C. Banuls, L. Pollet, I. Bloch, and S. Kuhr, Science **334**, 200 (2011).

[17] M. Cheneau, P. Barmettler, D. Poletti, M. Endres, P. Schauß, T. Fukuhara, C. Gross, I. Bloch, C. Kollath, and S. Kuhr, Nature **481**, 484 (2012).

[18] S. E. Hamann, D. L. Haycock, G. Klose, P. H. Pax, I. H. Deutsch, and P. S. Jessen, Phys. Rev. Lett., 4149 (1998).

[19] V. Vuletić, C. Chin, A. J. Kerman, and S. Chu, Phys. Rev. Lett. **81**, 5768 (1998).

[20] A. J. Kerman, V. Vuletic, C. Chin, and S. Chu, Phys. Rev. Lett. **84**, 439 (2000).

[21] D.-J. Han, S. Wolf, S. Oliver, C. McCormick, M. T. DePue, and D. S. Weiss, Phys. Rev. Lett. **85**, 724 (2000).

[22] A. M. Kaufman, B. J. Lester, and C. A. Regal, Phys. Rev. X **2**, 041014 (2012).

[23] Y. S. Patil, S. Chakram, L. M. Aycock, and M. Vengalattore, Phys. Rev. A **90**, 033422 (2014).

[24] J. D. Thompson, T. G. Tiecke, A. S. Zibrov, V. Vuletic, and M. D. Lukin, Phys. Rev. Lett. **110**, 133001 (2013).

[25] D. S. Weiss, J. Vala, A. V. Thapliyal, S. Myrgren, U. Vazirani, and K. B. Whaley, Phys. Rev. A **70**, 040302 (2004).

[26] J. W. Park, C.-H. Wu, I. Santiago, T. G. Tiecke, S. Will, P. Ahmadi, and M. W. Zwierlein, Phys. Rev. A **85**, 051602 (2012).

[27] S. Murmann, A. Bergschneider, V. Klinkhamer, G. Zürn, T. Lompe, and S. Jochim, Phys. Rev. Lett. **114**, 080402 (2015).

[28] A. M. Kaufman, B. J. Lester, C. M. Reynolds, M. L. Wall, M. Foss-Feig, K. R. A. Hazzard, A. M. Rey, and C. A. Regal, Science **345**, 306 (2014).

[29] C.-H. Wu, J. W. Park, P. Ahmadi, S. Will, and M. W. Zwierlein, Phys. Rev. Lett. **109**, 085301 (2012).